Hierarchically porous FER zeolite obtained via FAU transformation for fatty acid isomerization'

Applied Catalysis B: Environmental 263 (2020) 118356

Contents lists available at ScienceDirect

Applied Catalysis B: Environmental

journal homepage: www.elsevier.com/locate/apcatb

Hierarchically porous FER zeolite obtained via FAU transformation for fatty acid isomerization

Aleksei Bolshakov[a], Rim van de Poll[a], Tanja van Bergen-Brenkman[b], Sophie C.C. Wiedemann[b], Nikolay Kosinov[a], Emiel J.M. Hensen[a,*]

[a] Laboratory of Inorganic Materials and Catalysis, Department of Chemical Engineering and Chemistry, Eindhoven University of Technology, P.O. Box 513, 5600 MB, Eindhoven, the Netherlands
[b] Croda Nederland, B.V., PO Box 2, 2800 AA, Gouda, the Netherlands

ARTICLE INFO

Keywords:
Ferrierite
Hierarchical zeolite
FAU transformation
Dual-template
Fatty acid isomerization

ABSTRACT

Skeletal isomerization of linear unsaturated fatty acids is important in the production of branched-chain saturated fatty acids with diverse applications. This reaction can be efficiently catalyzed by ferrierite (FER) zeolite. The reaction, however, suffers from diffusion limitations in the 10-membered ring channels. Herein, we report a method for the synthesis of hierarchically porous FER zeolite via transformation of FAU precursor driven by N-methylpyrrolidine (NMP) and amphiphile 1,2-dimethyl-3-hexadecyl-1H-imidazol-3-ium bromide (C_{16}dMImz) as the structure-directing agent (SDA) and a mesoporogen, respectively, under hydrothermal conditions. This dual-template approach allows tuning the morphological and textural properties of the mesoporous FER materials by varying the concentration of the mesoporogen in the initial gel. The optimized FER sample is characterized by a high mesoporous volume (0.19 $cm^3\ g^{-1}$), large external surface area (~120 $m^2\ g^{-1}$) and reduced crystal size in the *a*- and *c*-dimensions. This implies shortened diffusional pathways in the 10-membered ring channels. These modifications led to a significantly enhanced catalytic performance of hierarchical FER zeolite in the isomerization of fatty acids in comparison with a bulk FER reference zeolite.

1. Introduction

The annual global production of oils (mainly palm, soybean and rapeseed) and (recycled) fats is estimated to be more than 160 million metric tonnes [1,2]. The use of these bio-based products can contribute to sustainability targets. Branched-chain saturated fatty acids (BSFA), which are typically iso-stearic acids, are widely used by the chemical industry for the production of personal care products and biodegradable lubricants [3–5]. The key advantages of such BSFA over unsaturated or linear fatty acids (FA) are their better thermal and oxidative stability and lower melting and cloud points [6,7]. One of common strategy to obtain iso-stearic acids is skeletal isomerization of unsaturated fatty acids (FA) such as oleic acid (OA) followed by hydrogenation [8].

Previous research has already shown the utility of acidic medium- and large-pore zeolites such as ZSM-5, Mordenite and Beta in catalyzing the isomerization of OA to branched products [3,6,9]. The limited space inside the micropores of zeolites hinders the formation of oligomeric products which would deactivate the catalyst [10]. Promising results for the OA isomerization reaction were described by Ngo et al., who used ferrierite (FER) zeolite as the catalyst [7]. In particular, it was possible to achieve a high OA conversion in combination with a good selectivity to branched-chain unsaturated fatty acids (BUFA) [3,11,12]. These BUFA are the intermediates to the formation of BSFA. Ferrierite (FER) is a medium-pore zeolite characterized by a two-dimensional (2D) pore system consisting of 10-membered ring (4.2 × 5.4 Å) channels intersected by 8-membered ring (3.5 × 4.8 Å) channels [13]. Typically, FER is synthesized by hydrothermal synthesis using appropriate silicon and aluminum sources and small structure directing agents (SDAs) in the form of organic molecules such as ethylenediamine [14] or pyrrolidine [15]. Another approach is to prepare ferrierite using zeolite Y (FAU) as a source of silicon and aluminum. This preparation is described as a transformation of FAU into FER, although the underlying transformation mechanism is not well understood [16–18].

The use of zeolites in which the pore diameters are usually much smaller than the zeolite crystals often leads to mass transport limitations. This is because the rate of intracrystalline diffusion can be slow compared to the rate of adsorption and desorption to/from the crystals. In particular, the formation of molecules that cannot diffuse out of the zeolite and therefore deactivate the catalyst is a common problem. A

* Corresponding author.
E-mail address: e.j.m.hensen@tue.nl (E.J.M. Hensen).

https://doi.org/10.1016/j.apcatb.2019.118356
Received 26 August 2019; Received in revised form 19 October 2019; Accepted 27 October 2019
Available online 11 November 2019

common approach to overcome such diffusion limitations is to reduce the crystal domain size of the zeolite and many methods have been established for this purpose [19–22]. The crystal size reduction is preferably brought about by introducing mesoporosity in zeolite crystals, either in top-down or bottom-up approaches. Thus, it may be expected that pore hierarchization of ferrierite can help to improve the performance for OA isomerization. In the former class, post-synthesis dealumination [23,24] and desilication [25,26] are efficient and easy to scale up, but drawbacks include poor control over acidic and textural properties of the final porous materials [27–30]. Alternatively, in a bottom-up approach the mesopores are introduced during the preparation of the zeolite crystals. There are many methods to achieve this, which often depend on the use of a mesoporogen in the zeolite synthesis gel. Typically, structure-directing agents are combined, one conventional SDA for zeolite formation (nanoscale structure direction) and another one to introduce intracrystalline mesopores (mesoscale structure direction). Several successful examples of this dual-templating strategy have been demonstrated [31–33]. Recently, several research groups obtained hierarchical FER using typical aluminum and silicon sources *such as* sodium silicate - aluminum sulfate and silica - sodium aluminate [34–37]. Important aspects to take into account in the further development of hierarchically-porous FER zeolites are the long hydrothermal synthesis of FER, usually exceeding two weeks, [34] the relatively high SDA concentration (SDA/Si ≥ 0.25) [36,38] and specific ageing steps [37,39].

In this work, we developed a method for the one-pot (bottom-up) synthesis of hierarchically porous FER zeolite via FAU reconstruction in the presence of N-methylpyrrolidine (NMP) and 1,2-dimethyl-3-hexadecyl-1H-imidazol-3-ium bromide (C_{16}dMImz) as, respectively, nano- and mesoscale SDAs. FAU was found to be an effective a silica-alumina precursor for preparation of microporous FER zeolite, templated by NMP in a synthesis of 8 days at 140 °C. The formation of FER took place via a layered intermediate phase. Addition of C_{16}dMImz in the initial gel resulted in mesoporous ferrierite (V_{meso} $0.09-0.28\ cm^3\ g^{-1}$) with high crystallinity and different morphologies depending on the concentration of C_{16}dMImz. Optimized hierarchically porous FER zeolite with strong Brønsted acidity displayed improved properties in the isomerization of fatty acids compared to microporous FER zeolite.

2. Experimental

2.1. Synthesis of chemicals

2.1.1. ,2-dimethyl-3-hexadecyl-1H-imidazol-3-ium bromide (C_{16}dMImz)

The synthesis of C_{16}dMImz was based on a procedure reported in the literature [40].

0.013 mol of 1-bromohexadecane (Sigma Aldrich, 98.0%) and 0.016 mol 1,2-dimethylimidazole (Sigma Aldrich, 97.0%) were dissolved in a 50 ml mixture of ethanol (Biosolve, 99.9%) and acetonitrile (Biosolve, 99.9%) (1 : 5 M ratio) and heated at 70 °C for 16 h under nitrogen atmosphere. After evaporation of the solvents and addition of diethyl ether (Biosolve, 99.5%), a white powder was seen to precipitate. The solid product was filtered and dried in a vacuum oven at 50 °C for 12 h. The purity of $C_{16}H_{33}$-[1,2-dimethyl-3-imidazolium] was verified by ^{1}H, ^{13}C, gHSQC and gCOSY NMR after dissolution in $CDCl_3$ (Fig. S1-S4). The product yield was 75%.

2.2. Synthesis of zeolites

N-methylpyrrolidine (NMP) and the bromide form of C_{16}dMImz were first dissolved in deionized water at room temperature. Then, a sodium silicate solution (Merck, SiO_2 27.0 %, Na_2O 8.0 %) was added dropwise to the template solution under stirring. Subsequently, NH_4Y zeolite (Alfa Aesar, SiO_2/Al_2O_3 of 5.2) was suspended in the obtained mixture followed by vigorous stirring for 4 h at ambient temperature. The molar composition of the synthesis gel was (1-*x*) NMP: *x* C_{16}dMImz: 1.82 Na_2O : 0.25 Al_2O_3 : 7.7 SiO_2 : 231 H_2O (*x* = 0.01 - 0.25). The resulting gel was transferred into a 45 ml Teflon-lined stainless-steel autoclave and heated at 125 °C for 264 h under rotation (50 rpm). These zeolites were denoted as FER-*x* (*x* = 0.01, 0.025, 0.05, 0.1, 0.15, 0.20, 0.25) in accordance with the amount of the mesoporogen that partially substitutes NMP. A conventional bulk FER zeolite was synthesized from the same gel without addition of C_{16}dMImz (*x* = 0, FER-C) followed by hydrothermal synthesis at 140 °C for 192 h under rotation at 50 rpm. The resulting solid product was filtered, thoroughly washed with deionized water until pH < 8, and dried in air at 110 °C overnight before calcination in the air at 550 °C (1 °C/min) for 7 h.

2.3. Catalyst preparation

Na-FER samples were converted to the proton form by ion exchange, which was performed in three consecutive steps with fresh aqueous 1.0 M NH_4NO_3 solutions (1 g of the solid per 100 ml of the solution, 3 h, 70 °C). Then, the ammonium form of the product was separated from the solution via centrifugation followed by drying at 110 °C and calcination at 550 °C for 5 h (heating rate of 0.9 °C/min), in order to obtain the final proton form (H-FER).

2.4. Characterization

Basic Characterisation: The crystallinity and phase purity of all samples were determined by X-ray diffraction (XRD). XRD patterns were collected on a Bruker D_2 Endeavour powder diffraction system with Cu Kα radiation. Patterns were obtained in the 2θ range of 5–60°, with a step size of 0.02° and duration of 0.4 s. Textural properties were examined through Ar physisorption. Adsorption and desorption isotherms were measured at −186 °C on a Micrometrics ASAP-2020 machine. The powders were outgassed at 400 °C with a residual pressure of 5 μbar for 8 h prior to measurement. The microporous volume was calculated by the *t*-plot method using the 3.5–7.5 Å thickness range. The mesoporous volume was determined from the adsorption branch of the isotherms by the Barrett − Joyner − Halenda (BJH) method. The total pore volume was recorded at $P/P_0 = 0.95$. The elemental composition of aluminium-containing products was determined by ICP-OES (inductively coupled plasma optical emission spectroscopy) through a Spectro CIROS CCD ICP spectrometer with axial plasma viewing. For these measurements the samples were dissolved in a 1:1:1 (by weight) mixture of HF (40 %) : HNO_3 (60 %) : H_2O. Thermogravimetric analysis (TGA) analysis was performed on a Mettler Toledo TGA/DSC 1 instrument. About 10 mg of the sample was placed in an alumina crucible. The uncovered crucible was heated to 750 °C at a rate 5 °C /min in 40 ml/min He and 20 ml/min O_2 flow.

Electron Microscopy: Scanning electron microscopy (SEM) micrographs were obtained using a FEI Quanta 200 F instrument with an acceleration voltage of 3 kV and a spot size of 4.5 Transmission electron microscopy (TEM) images were recorded on a Tecnai 20 (type Sphera, FEI, now Thermo Fischer Scientific) operated at 200 kV. TEM sample preparation involved sonication of the samples in pure ethanol (Biosolve, extra dry, 99.9%) and applying a few droplets of the suspension to a 200 mesh Cu TEM grid with a holey carbon support film. JmageJ software was used to determine a size of ferrierite crystals and lattice parameters.

IR Spectroscopy: IR spectra of the zeolites were recorded on a Bruker Vertex 70v FTIR spectrometer in the range of $4000-400\ cm^{-1}$. The spectra were acquired at a $2\ cm^{-1}$ resolution, as an average of 64 scans. The samples were prepared as thin wafers of 10 − 12 mg with a diameter of 13 mm and placed inside a controlled-environment transmission IR cell. The samples were then activated at 550 °C (2 °C/min) in air flow for 3 h before cooling the cell to 150 °C and measuring the spectra under vacuum. Pyridine was then introduced into the IR cell from an ampoule kept at room temperature. After exposure for 10 min. to pyridine (enough to reach equilibrium), the sample was evacuated

over three consecutive 1 h periods at 150 °C, 300 °C and 500 °C, with a spectrum taken after each hour and cooled to 150 °C. The spectra were normalized by the weight of the wafer.

NMR spectroscopy: Magic angle spinning (MAS) nuclear magnetic resonance (NMR) spectra were performed at room temperature with a 11.7 T Bruker DMX500 NMR spectrometer operating at 500 MHz for ^{1}H and 132 MHz for ^{27}Al. ^{27}Al MAS-NMR spectra were recorded with a spinning rate of 25 kHz and a single excitation pulse length of 1 µs with a 1 s repetition time. ^{27}Al 3QMAS NMR spectra were recorded by use of the three-pulse sequence p_1-t_1-p_2-τ-p_3-t_2 for triple-quantum generation and zero-quantum filtering (strong pulses p_1 = 3.4 µs and p_2 = 1.4 µs at v_1 = 100 kHz; soft pulse p_3 = 11 µs at v_1 = 8 kHz; filter time τ = 20 µs; interscan delay 0.2 s). The ^{1}H measurement was carried out using a 4 mm MAS probe head with sample rotation rate of 10 kHz. ^{1}H NMR spectra were recorded with a Hahn-echo pulse sequence p_1-τ_1-p_2-τ_2-aq with a 90° pulse p_1 = 5 µs and a 180° p_2 = 10 µs. The interscan delay was set to 120 s for quantitative spectra. ^{1}H NMR shifts were calibrated using tetramethylsilane (TMS) and a saturated aqueous $Al(NO_3)_3$ solution was used for ^{27}Al NMR shift calibration. Prior to ^{1}H NMR measurement, the zeolite sample was dehydrated at 400 °C and 5 µbar pressure for 8 h.

2.5. Skeletal isomerisation of fatty acids

The liquid-phase isomerisation of FA to BUFA was chosen as a model reaction to determine the catalytic performance of the synthesized H-FER zeolites (Scheme 1).

The FA mixture with the trade name Priolene™ 6926 (Croda), composed of 88–89% oleic (OA), 5–6% palmitic, 3–4% linoleic (LA), < 0.5% α-linolenic (ALA) and ~2% stearic (SA) acid was supplied by Croda. The isomerisation reaction was carried out in a 50 ml mini-PARR® autoclave (Series 5500 High Pressure Compact) equipped with a 4848 Reactor Controller (Parr Instrument Company). After purging with nitrogen three times, the FA mixture (25 g), H-FER catalyst (0.25 g) and demineralised water (0.4 g) were mixed together, and then the system was pressurised with nitrogen to ~1 bar. The reaction took place at a stirring rate of 800 rpm and a temperature of 260 °C (heating rate of ~7 °C/min), which leads to a pressure of ~6.5 bar in the autoclave. After completing the activity test (between 0.42 and 6 h), the reactor was cooled to below 80 °C and the reaction mixture was separated from the zeolite catalyst by filtration.

Analysis of products: The composition of the crude reaction mixtures was determined using high-temperature GC (HT-GC). The GC was equipped with a cold on-column injection and a metal column with a non-polar stationary phase Cp-SimDist Ultimetal (Chrompack WCOT, 5 m x0.53 mm x0.17 µm) and the components were detected with a flame ionisation detector (FID) based on retention time. The carrier gas was N_2 with a constant flow of 10 mL/min. The temperature program was as follows: initial temperature of 60 °C, hold for 1 min; temperature increase of 30 °C/min until 150 °C; hold 0 min; temperature increase of 12 °C/min until 375 °C; hold 5 min. The detector was operated at 375 °C. The injection volume was 1 µL for a concentration of 10 mg/mL. The hydrogenated monomer fractions were analyzed by GC after methylation. The GC was equipped with a split injection and a fused silica capillary column with a polar stationary phase FFAP-CB (Chrompack WCOT, 25 m x0.32 mm x0.30 µm), and the components detected with FID based on retention time. The carrier gas was H_2 with a constant pressure of 8 Psi, an inlet temperature of 275 °C and a split ratio of 1/30. The temperature program used was: initial temperature of 120 °C, hold for 0 min; temperature increase of 8 °C/min until 250 °C; hold 7 min. The detector was set at 275 °C. The injection volume was 1 µl for a concentration of 10 mg/mL.

Taking into account the large difference in molecular weight of as-synthesized products, their determination required two further steps. The oligomer concentration was directly determined from the crude reaction mixture by high-temperature gas chromatography GC. The monomer fraction was then separated from the crude reaction mixture by vacuum distillation at 260 °C at a pressure lower than 1 mbar). To use the GC method for BUFA characterization, the fatty acids were preliminarily converted to their respective methyl esters according to ISO 12966-2:2017 method. Firstly, the aliquots of the monomer fraction were diluted in ethyl acetate and hydrogenated *in situ* over Adam's catalyst (PtO_2, Sigma Aldrich, Pt 80–85%) at 25 °C. After solvent evaporation, the saturated acids were then methylated with BF_3/methanol to the Corresponding esters.

The initial mass fraction of the oleic ($\chi_{OA,0}$), linoleic ($\chi_{LA,0}$) and α-linolenic ($\chi_{ALA,0}$) acids (including positional and *cis/trans* isomers) were considered as the reactive components of the FA mixture. Their mass conversion ($X_{FA,t}$) is determined by quantification of the mass fraction of stearic acid ($\chi_{SA,t}$) in the hydrogenated monomer fraction as a function of time (t) and is given by

$$X_{FA,t} = 1 - \frac{[(\chi_{SA,t} + \chi_{OA,t}) \times Y_{M,t} - \chi_{SA,0}]}{[\chi_{OA,0} + \chi_{LA,0} + \chi_{ALA,0}]} \quad (1)$$

The onset of the reaction (t = 0) is the time at which the temperature reached 260 °C. ($Y_{M,t}$) is the distillation yield of the monomeric species determined by HT-GC analysis and ($\chi_{SA,0}$) the amount of unreacted stearic acid in the initial FA mixture. The selectivity towards BUFA ($S_{B,t}$) was derived from the mass fraction of all hydrogenated BUFA ($\chi_{BUFA,t}$) in the hydrogenated monomer fraction. Again, a correction was made for the distillation yield of the monomeric species ($Y_{M,t}$):

$$S_{B,t} = \frac{[\chi_{BUFA,t} \times Y_{M,t}]}{[(\chi_{OA,0} + \chi_{LA,0} + \chi_{ALA,0}) \times X_{FA,t}]} \quad (2)$$

3. Results and discussion

3.1. FAU to FER transformation in the presence of NMP

In the current work we employed a synthesis approach where faujasite (NH_4-FAU, Si/Al 2.6) and sodium silicate were used as silica-

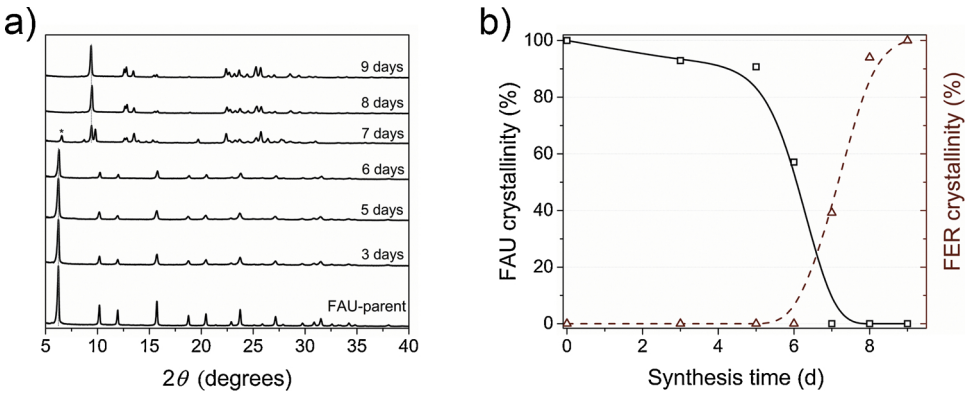

Fig. 1. a) XRD patterns of calcined samples obtained as a function of synthesis time. b) Crystallinity changes of FAU and FER phases during zeolite synthesis (relative crystallinity of the samples was calculated as changes in the area of the diffraction peak at $2\theta = 6.2°$ for FAU and $2\theta = 9.5°$ for FER, respectively; the peak areas at $2\theta = 6.2°$ and $2\theta = 9.5°$ of respectively the parent NH_4-FAU and bulk FER zeolite were taken as reference values).

alumina and silica sources, respectively, to obtain FER zeolite. Fig. 1 shows XRD patterns as a function of the synthesis time for the synthesis of bulk FER zeolite (FER-C) in the presence of NMP at 140 °C. The contributions of FAU and FER phases are indicated. After 6 days of the synthesis, FAU is the only crystalline phase present. During the first 5 days, only a minor decrease in the amount of FAU is observed by XRD. The first indication of the presence of FER zeolite is after 7 days and the sample is fully crystalline after another day of synthesis (Fig. 1a). Based on literature, it is likely that slow dissolution of the starting zeolite produces locally ordered aluminosilicate blocks containing five-ring building units needed for the crystallization of FER zeolite [41,42].

When the concentration of such units becomes high enough, ferrierite starts crystallizing driven by the organic SDA. As shown in our previous work, the hydrothermal synthesis at a nearly similar gel composition and crystallization conditions (140 °C, 6 days) but without NMP as the SDA led to the formation of mordenite (MOR) zeolite [43]. FER seeds were also successfully applied to direct the inter-zeolite conversion of ultra-stable Y zeolite to FER at 150 °C [18,42]. Using Al $(OH)_3$ instead of FAU as Al source resulted first in MOR zeolite after a short synthesis time, followed by ferrierite formation, which started after 5 days (Fig S5 and S6). It is therefore important to ensure a slow release of alumina-containing species from the FAU precursor into the reaction mixture to selectively crystallize FER zeolite.

The obtained samples were further examined by electron microscopy (Figs. 2 and 3). The starting FAU zeolite consists of typical octahedral crystals [44] with a size smaller than 1 µm. The first morphology changes were observed after 5 days of hydrothermal synthesis, when a layered material (Fig. S7a) was seen on the surface of FAU crystals (Fig. 2c). The interlayer distance of this phase of about ~1.1 nm is similar to that of PREFER, which is a known lamellar precursor of FER [45,46]. Further, we detected an intermediate XRD-invisible flake-like phase (Fig. 2d and 3 b), which is composed of PREFER sheets and faujasite fragments (Fig. S7b). After 7 days of hydrothermal synthesis, two phases were found: agglomerated FER sheets (Fig. 2e) and plate-like precursors (Fig. 3c), which are characterized by an interlayer distance of ~1.3 nm (Fig. S7c), which is underpinned by the XRD peak at $2\theta = 6.6°$ (Fig.1a). The complete conversion into pure FER sheet-like aggregates occurred rapidly during another day of synthesis (Figs. 2f and 3 d). Prolonged synthesis for 9 days did not lead to further morphological changes (Fig. S8). These results are in agreement with a work of Okubo and co-workers, [41] who showed the importance of the formation of a plate-like precursor (containing 5-membered ring units) prior to the fast crystallization of ferrierite.

Thermogravimetric analysis revealed the presence of NMP molecules inside the pores (combustion temperature > 300 °C) [47,48] of the obtained FER samples after 7 days of hydrothermal synthesis (Fig. 4). Materials obtained after a shorter synthesis times showed a main weight loss feature below 150 °C (Fig. 4a), corresponding to the desorption of water from the pores of faujasite [49]. These findings support the XRD results, where the FER phase stabilized by NMP was only obtained after 7 days of synthesis. After 8 days, the crystallization of the FER phase was complete and the amount of organics in the pores determined by TGA was 12 wt%. Altogether, XRD, electron microscopy and TG results demonstrate a picture of FER synthesis, taking place by (i) slow dissolution of FAU, (ii) formation of an intermediate PREFER phase and (iii) quick crystallization and growth of FER crystals. Textural and acidic properties of the FER zeolite after 8 days of synthesis will be discussed below. This sample was chosen as a reference because longer treatment time did not result in significant improvements in terms of crystallinity or morphology.

3.2. Hierarchical ferrierite zeolite

To introduce mesoporosity in microporous FER, we applied a dual-templating approach [31,33] where two SDAs cooperate under hydrothermal conditions to obtain a hierarchically porous material. In the current study, an imidazolium-based surfactant was chosen due to its ability to stabilize the FER framework [50] and with a view of exploring the suitability of the imidazole molecule as a commercially available intermediate for template synthesis. Preliminary experiments showed formation of non-uniform FER crystals when the synthesis was carried out at 140 °C (Fig. S9). By lowering the crystallization temperature to 125 °C, more uniform crystals were obtained. Highly crystalline and phase-pure FER zeolites were obtained by substitution of NMP for C_{16}dMImz in the range of 1 − 25 mol% (samples denoted as FER − 0.01–FER − 0.25) after 11 days of hydrothermal synthesis (Fig. 5a). As compared to conventional FER-C, obtained samples revealed changes in the width and intensity of the diffraction lines in particular at 2θ ~9.5° corresponding to the [200] planes (Fig. 5b). A decreasing intensity of [200] reflection at higher C_{16}dMImz concentrations (≥5%) accompanied by peak broadening can be attributed to the reduction of the crystalline domain size in the *a*-direction of the FER crystals.

Investigation of the obtained samples by SEM and TEM showed a strong correlation between the concentration of C_{16}dMImz in the initial gel and the morphology of the final materials (Figs. 6 and 7). Reference FER-C sample displayed crystals with a 0.5–0.7 µm size and can be

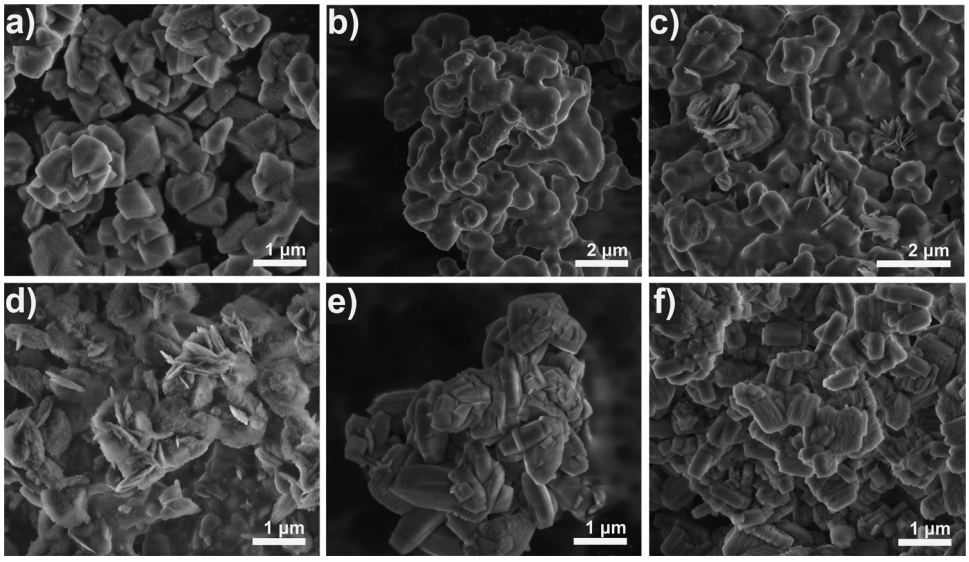

Fig. 2. SEM micrographs of a) parent FAU and the calcined samples obtained at different synthesis time: b) 3 days, c) 5 days, d) 6 days, e) 7 days and f) 8 days.

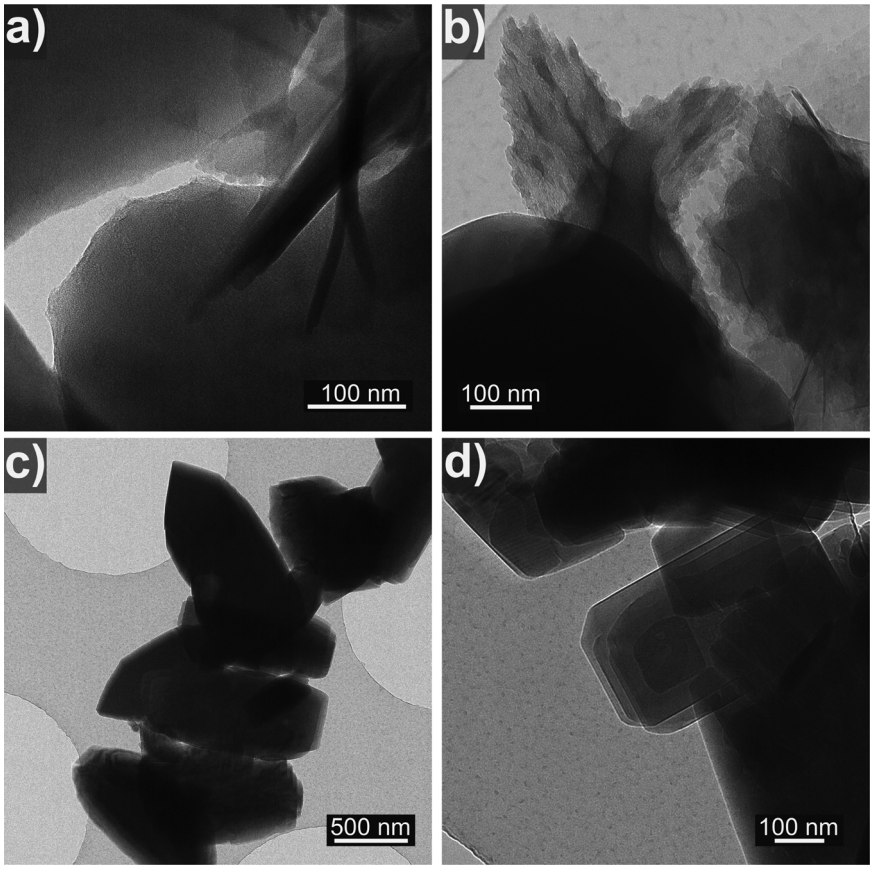

Fig. 3. TEM micrographs of the calcined samples obtained at different synthesis time: a) 5 days, b) 6 days, c) 7 days and d) 8 days.

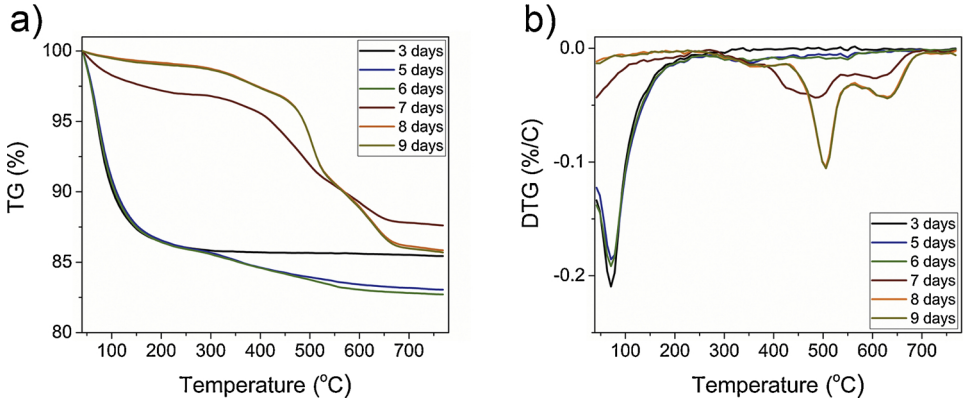

Fig. 4. a) Thermogravimetric analysis (TGA) and b) derivative thermogravimetry (DTG) of the as-synthesized FER samples obtained at different synthesis time.

considered as an agglomeration of sheets (Fig. 6a and 3 d).

Lattice distances of 0.71 nm and 0.94 nm (Fig. S10a-d) attributed to [020] and [200] planes, respectively, point to crystals oriented along the *c*-axis with a length of ~500 nm (Fig. 7a–c and Scheme S1). The presence of a minor amount of C_{16}dMImz leads to changes of crystals growth in *a*- and *b*-directions (Figs. 6b,c) and 7 b,c) and Table S1), combined with the decreased width of the sheets from ~40 nm to ~25 nm (Figs. 8 and S10b,c). In this case, the imidazole head group is likely located in the larger 10-membered ring channels, [51] whereas the hydrophobic tail enables spacing the stacked crystals in the agglomerates, preventing crystal growth in the *c*-direction. Further substitution of NMP with C_{16}dMImz up to 10 % resulted in a further decrease of the crystal size in *a*- and *b*-directions (Figs. 6d,e) and 7 d,e) with the formation of tile-like particles of ~120 nm in width and a thickness of ~9 – 15 nm (Figs. 8 and S10d,e), Table S1). This behavior can be explained by the strong stabilization of Al species placed in 8-membered ring pockets or channel intersections by the imidazolium cation [50]. Thus, the hydrophobic tail might be located outside the small 8MR channels, thereby preventing sheet growth in the b-direction. The relatively small amount of NMP SDA involved in the formation of FER supports this hypothesis. Indeed, a synthesis with a 10% substitution level of NMP with C_{16}dMImz and a lower total SDA/Si ratio (0.1 vs. 0.13) did not lead to the successful transformation of FAU to FER (Fig. S11).

The FER – 0.15 sample consists of agglomerated sheets (~40 nm thickness, ~300 nm width) (Fig. 7f) constructed by individual ones of ~8 nm size (Fig. S10f). The electron microscopy images are consistent with the XRD results and confirm significant changes in the crystal size after 5 % NMP substitution with C_{16}dMImz. Increased concentration of C_{16}dMImz led to the collapse of the plate-like particles to a non-uniform

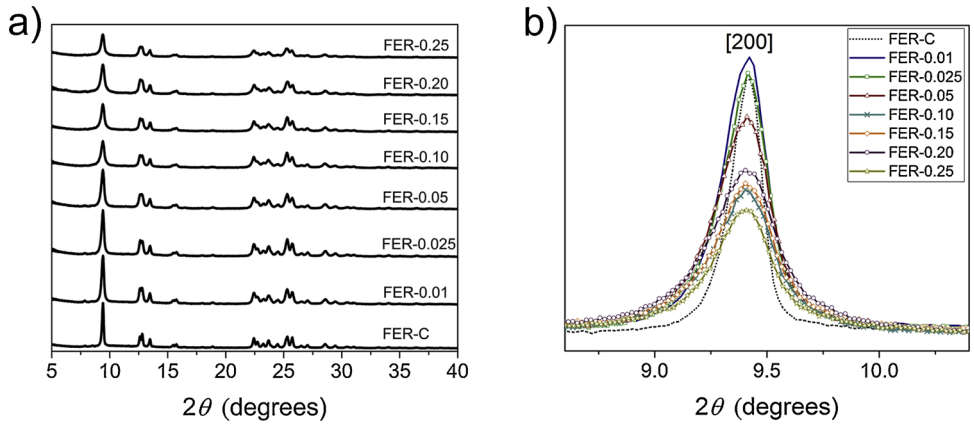

Fig. 5. XRD patterns of the ferrierite samples at different substitution levels of NMP with C_{16}dMImz: a) wide-angle range, b) zoom of the 2θ = 8.5–10.5° range.

crushed structure (Fig. 6g, h), the material nevertheless remaining purely FER.

FER samples with uniform structures were analyzed for their textural properties by Ar physisorption. The isotherm of conventional FER zeolite has the type I shape, which is typical for microporous materials, while the FER − 0.01–FER-0.15 samples displayed the type IV isotherm (Fig. 9a) [52,53]. The latter one is characterized by a hysteresis loop at higher pressure, which is due to capillary condensation in the mesopores. The high crystallinity of the calcined materials was confirmed by a high microporous volume (0.08 − 0.11 cm^3 g^{-1}). We found a linear correlation between the percentage of substituted NMP in the initial gel and the mesoporous volume and external surface area of the final materials (Fig. 9b). This relation is valid up to C_{16}dMImz/Si = 0.01 and leads to maximum values of V_{meso} = 0.28 cm^3 g^{-1} and S_{ext} = 181 cm^2 g^{-1}. Following an increase in the concentration of C_{16}dMImz resulted in a decrease of both parameters (Table 1), which can be explained by the complex structure of the sheets effecting their local intergrowths. The pore size distributions derived from *NLDFT*-method show a broad distribution of mesopores (3 − 50 nm) for all mesoporous materials (Fig. S12).

The FER samples are characterized by similar Si/Al ratios of ~10 according to ICP-OES elemental analysis (Table S2). The local environment of aluminum in the samples was determined by ^{27}Al MAS NMR spectroscopy (Fig. 10).

The FER materials exhibited two resonances at ~54 ppm and at ~0 ppm, which can be attributed to framework (Al^{IV}) and extra-framework (Al^{VI}) types of Al, respectively [54]. The deconvoluted spectra showed that the Al atoms were mainly incorporated in the framework (> 80% for all samples) (Fig. 10 and Table S2). Additionally, ^{27}Al MQ MAS NMR analysis was performed to investigate the variation of the local chemical environment of each Al species [55] after introduction of mesoporosity (Fig. S13). The tetrahedral region 40 − 60 ppm consists of only one component, pointing to the absence of penta-coordinated Al. At the same time, the broadening of the main signal parallel to the isotropic axis (F1) may be related to a different environment of Al^{IV} such as distorted Al species formed during the calcination process [25,56,57].

We used IR spectroscopy for the characterization of the acidic properties of the obtained samples. The IR spectra show stretching OH vibrations of different nature (Fig. 11). Detected bands are attributed to four types of hydroxyls: (i) terminal silanol groups at 3745 cm^{-1}, (ii) internal Si − OH at 3719 cm^{-1}, (iii) − OH attached to extraframework aluminum (EFAl) at 3647 $cm^{-1}$and (iv) bridging hydroxyl groups (Si − OH-Al) at 3600 cm^{-1} [51,58–60]. Notably, the amount of external silanols at 3745 cm^{-1} was higher after replacing NMP with more than 5% C_{16}dMImz in the initial gel. This effect can be explained by the significant morphological changes, amongst others the reduction of crystal size and the associated formation of more external surface.

Pyridine was chosen as a probe molecule for the quantification of the acidity of H-FER zeolites. Interaction of pyridine with different types of acid sites resulted in the appearance of several N−H bands: the bands at 1545 cm^{-1} and 1455 cm^{-1} relate to strong Brønsted acid sites

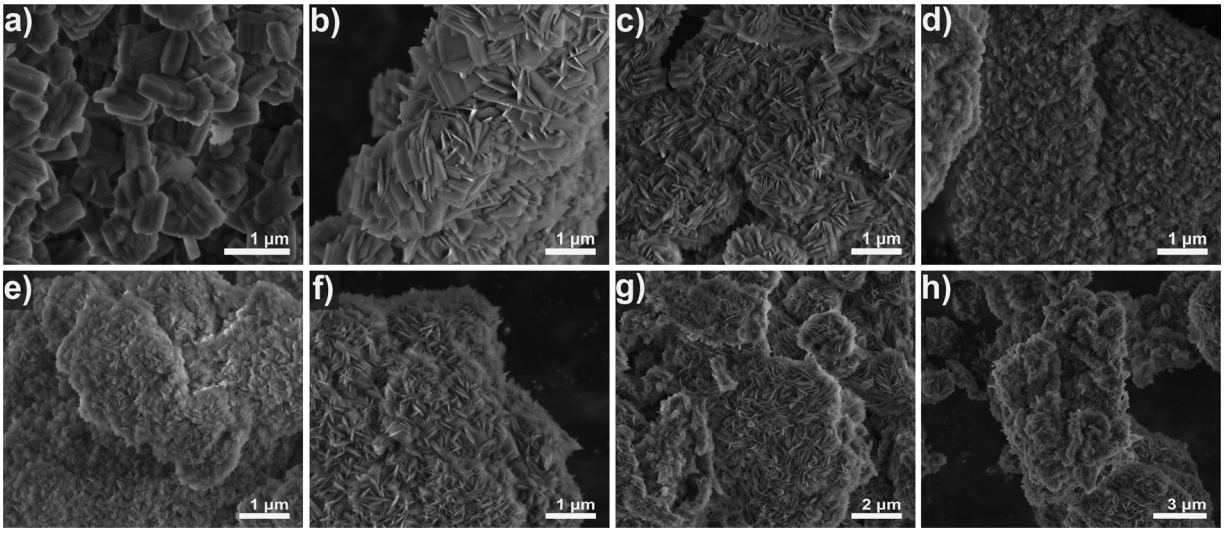

Fig. 6. SEM micrographs of calcined FER zeolites: a) FER-C, b) FER − 0.01, c) FER-0.025 d) FER − 0.05, e) FER − 0.10, f) FER-0.15, g) FER − 0.20 and h) FER − 0.25.

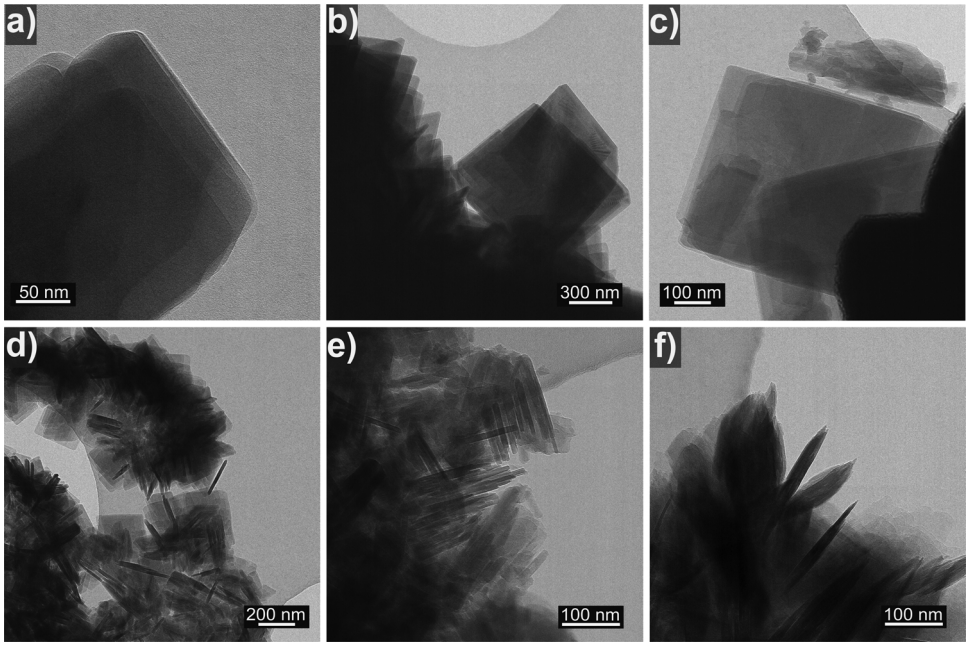

Fig. 7. TEM micrographs of calcined FER zeolites: a) FER-C, b) FER-0.01, c) FER-0.025 d) FER − 0.05, e) FER − 0.10 and f) FER − 0.15.

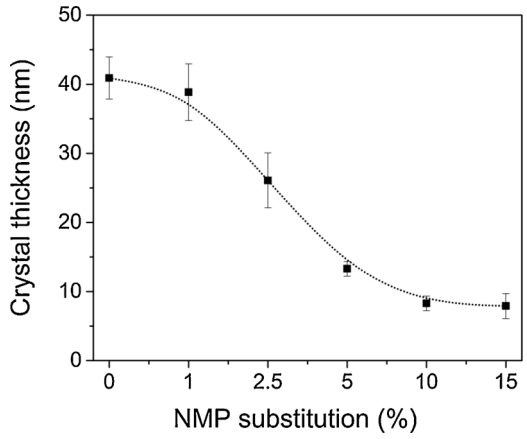

Fig. 8. Average thickness of FER sheets determined by TEM as a function of molar substitution level of NMP with C_{16}dMImz in the initial gel.

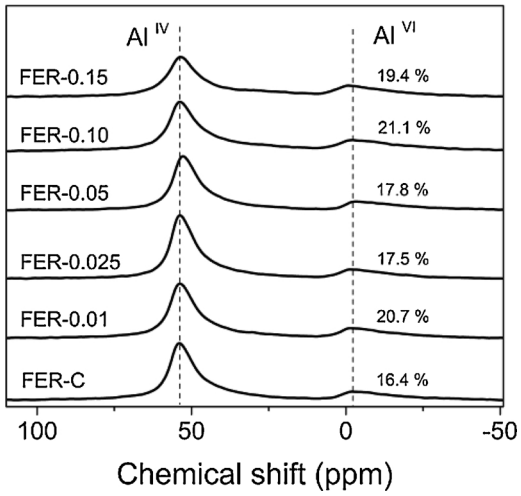

Fig. 10. ^{27}Al MAS spectra of the proton forms of FER zeolites (spectra are normalized by sample weight).

(BAS) and Lewis acid sites (LAS), respectively (Fig. S14) [61,62]. The band at 1490 cm^{-1} arises from pyridine molecules adsorbed on either of these acid sites [63,64]. Taking into account that pyridine molecules with a kinetic diameter of about 5.7 Å [65] cannot penetrate the small 8-membered ring FER channels (3.5 × 4.8 Å), pyridine adsorption can only take place on acid sites in 10-membered ring channels and at the external surface of the zeolites [63,66]. Fig. 12 displays a comparable quantity of BAS available to pyridine at low concentration of the

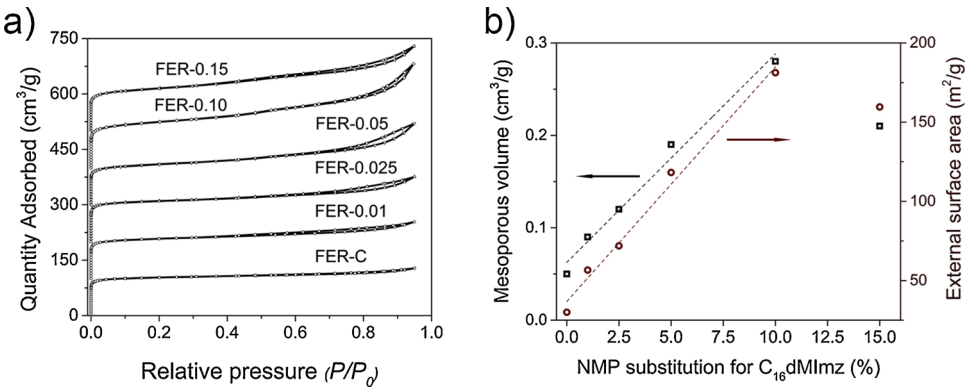

Fig. 9. a) Ar physisorption isotherm of calcined FER samples at different concentration of C_{16}dMImz (the isotherms were vertically offset by equal intervals of 100 cm^3 g^{-1}); b) Correlation between amount C_{16}dMImz in the initial gel and textural properties of the final.

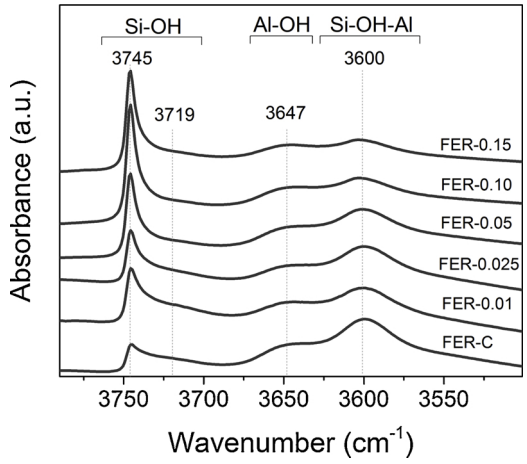

Fig. 11. IR spectra of various FER samples (spectra normalized to the sample weight).

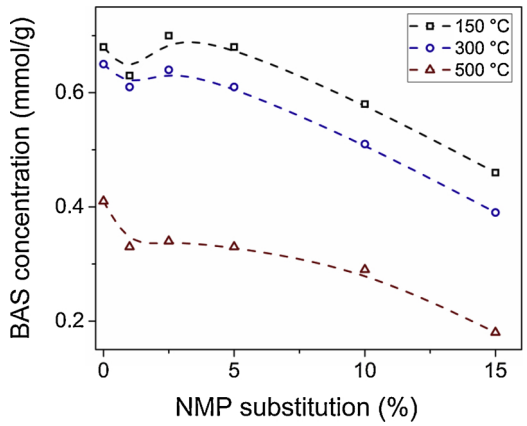

Fig. 12. Concentration of BAS in the H-FER samples as a function of the molar substitution level of NMP with C_{16}dMImz in the initial gel.

C_{16}dMImz (≤5% substitution level). A larger amount of C_{16}dMImz leads to a decrease of the density of BAS by ~40% for FER-0.15 sample.

Further, ^{1}H MAS NMR spectroscopy was employed to estimate the total acidity of FER samples. Analysis of ^{1}H NMR spectra of dehydrated samples revealed the presence of two types of Si-O(H)-Al groups: signals with chemical shifts of 4.1 ppm and 5.4 ppm are attributed to, respectively, isolated [47] and hydrogen-bonded bridged hydroxyls [67,68] (Fig. S15b). The acidity is in keeping with the pyridine desorption data obtained by IR spectroscopy: the amount of BAS remained the same up to 5 % of substitution of NMP with C_{16}dMImz in the initial gel followed by a decrease by ~40% when the substitution level is increased (Table S3). The reduction in the number of BAS at high C_{16}dMImz concentration is likely due to the dehydroxylation during calcination of FER zeolites accompanied by the formation of LAS [69,70]. Such LAS cannot be observed by ^{1}H NMR spectroscopy (Fig. S15a), but were partially detected in IR spectra of adsorbed pyridine (Table S3).

3.3. Skeletal isomerisation of fatty acids over H-FER catalyst

The fatty acids (FA) mixture, which contains about 90 wt% oleic acid (OA), was isomerized at 260 °C over the proton form of the H-FER samples (Scheme 1). Fig. 13a shows the conversion of the FA mixture as a function of the reaction time. Mesoporous FER – 0.01–0.05 catalysts converted the reaction mixture faster compared to a conventional FER. The highest conversion of 71% was reached after 6 h with FER – 0.05. Taking into account a comparable concentration of acid sites in the catalysts as judged by pyridine desorption, we attribute the distinct catalytic behavior of hierarchically porous FER zeolites to the improved mass transport. The FER samples obtained at a higher concentration of C_{16}dMImz (≥10% substitution level) are characterized by a much lower accessible acidity (Fig. 12), which has a negative effect on the catalytic performance. The high monomer yields in the crude product (95 ± 2%) found for all tested materials point to a minor contribution of external acid sites, which catalyze undesired dimerization and oligomerization side-reactions (Fig. S16) [71,72]. The formed (poly)enylic carbocations eventually block the pore entrances and, as a consequence, retard the isomerization process. We propose that a large fraction of BAS that are close to the external surface are located in the pore mouth of 8MR channels and not accessible for the bulky reactants [12]. The optimal FER-0.05 catalyst possesses a high "effective" acidity (Fig. S17) combined with good accessibility of BAS through 10-membered ring channels, which allowed reaching a BUFA yield of 52% (Fig. 13b).

4. Conclusions

We report a strategy to convert a FAU precursor into bulk FER zeolite using NMP as a SDA as well as hierarchically porous FER zeolite by adding an imidazole-based surfactant. Bulk ferrierite zeolite can be obtained after 8 days of hydrothermal synthesis at 140 °C via a transformation of NH_4-FAU precursor in the presence of NMP. Using FAU zeolite instead of other typical aluminum sources such as $Al(OH)_3$ prevents the formation of MOR as a side-phase due to the slow release of Al species during the crystallization process. Several stages of the conversion FAU to FER at hydrothermal conditions were observed: slow dissolution of FAU, development of a layered intermediate phase (PREFER) and quick growth of FER crystals. Partial substitution of NMP for C_{16}dMImz in the initial gel led to the development of the mesoporosity in FER crystals after 11 days at 125 °C. Varying the C_{16}dMImz

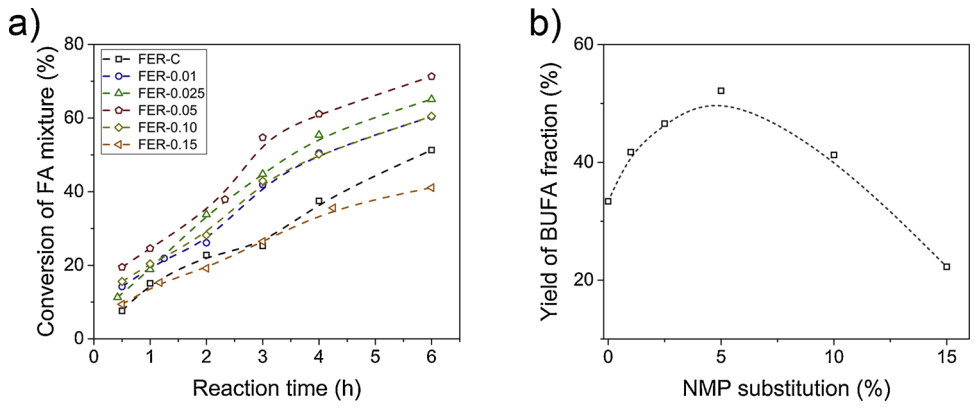

Fig. 13. a) Catalytic conversion of FA mixture (X_{FA}) over as-synthesized FER samples at 260 °C and b) yield of BUFA fraction after 6 h of the reaction.

concentration allows controlling morphology, textural and acidic properties of the hierarchical FER zeolites. Hierarchically porous FER materials show an advantage over bulk FER in terms of the isomerization of fatty acids. The optimal catalyst is FER-0.05 (V_{meso} 0.19 $cm^3 g^{-1}$, $S_{ext} \sim 120\ m^2\ g^{-1}$) displaying a much higher BUFA yield due to the increased mass transport and proper acidic properties.

Declarations of Competing Interest

We declare that the submitted work has not been published previously, that it is not under consideration for publication elsewhere, that its publication is approved by all authors and tacitly or explicitly by the responsible authorities where the work was carried out, and that, if accepted, it will not be published elsewhere in the same form, in English or in any other language, including electronically without the written consent of the copyright-holder.

Acknowledgments

The authors thank the TU/e Impuls program for financial support.

Appendix A. Supplementary data

Supplementary data associated with this article can be found, in the online version, at https://doi.org/10.1016/j.apcatb.2019.118356.

References

[1] F.D. Gunstone, The major sources of oils and fats, Oils and Fats in the Food Industry 7 (2009), pp. 11–25.
[2] J. Fry, C. Fitton, The importance of the global oils and fats supply and the role that palm oil plays in meeting the demand for oils and fats worldwide, J. Am. Coll. Nutr. 29 (2010) 245–252.
[3] Z.C. Zhang, M. Dery, S. Zhang, D. Steichen, New process for the production of branched-chain fatty acids, J. Surfactants Deterg. 7 (2004) 211–215.
[4] H.L. Ngo, R.O. Dunn, B. Sharma, T.A. Foglia, Synthesis and physical properties of isostearic acids and their esters, Eur. J. Lipid Sci. Technol. 113 (2011) 180–188.
[5] H. Wagner, R. Luther, T. Mang, Lubricant base fluids based on renewable raw materials: their catalytic manufacture and modification, Appl. Catal. A Gen. 221 (2001) 429–442.
[6] T.A. Foglia, T. Perlstein, Y. Nakano, G. Maerker, Process for the Preparation of Branched Chain Fatty Acids and Esters, (1983).
[7] H.L. Ngo, A. Nunez, W. Lin, T.A. Foglia, Zeolite-catalyzed isomerization of oleic acid to branched-chain isomers, Eur. J. Lipid Sci. Technol. 109 (2007) 214–224.
[8] L. Ha, J. Mao, J. Zhou, Z.C. Zhang, S. Zhang, Skeletal isomerization of unsaturated fatty acids on Beta zeolites: effects of calcination temperature and additives, Appl. Catal. A Gen. 356 (2009) 52–56.
[9] L. Kim, M.A. Us, J. Joseph, M.A. Us, F. Vinod, L.V. Dipietro, M.A. Us, J. Gregory, Patent Application Publication US 2003/0191330, (2003).
[10] M. Hunger, Catalytically active sites: generation and characterization, in: J. Čejka, A. Corma, S. Zones (Eds.), Zeolites and Catalysis, Synthesis, Reactions and Applications, Wiley-VCH Verlag GmbH & Co., KGaA, 2010, pp. 493–546.
[11] S.C.C. Wiedemann, Z. Ristanovic, G.T. Whiting, V.R. Reddy Marthala, J. Kärger, J. Weitkamp, B. Wels, P.C.A. Bruijnincx, B.M. Weckhuysen, Large ferrierite crystals as models for catalyst deactivation during skeletal isomerisation of oleic acid: evidence for pore mouth catalysis, Chem. Eur. J. 22 (2016) 199–210.
[12] S.C.C. Wiedemann, A. Muñoz-Murillo, R. Oord, T. Van Bergen-Brenkman, B. Wels, P.C.A. Bruijnincx, B.M. Weckhuysen, Skeletal isomerisation of oleic acid over ferrierite: influence of acid site number, accessibility and strength on activity and selectivity, J. Catal. 329 (2015) 195–205.
[13] L.B. McCusker, D.H. Olson, C. Baerlocher, Atlas of Zeolite Framework Types, (2007).
[14] High-silica zeolites of the ferrierite family, Stud. Surf. Sci. Catal. 33 (1987) 217–232.
[15] A.B. Pinar, P.A. Wright, L. Gómez-Hortigüela, J. Pérez-Pariente, Synthesis of ferrierite zeolite with pyrrolidine as structure directing agent: a combined X-ray diffraction and computational study, Microporous Mesoporous Mater. 129 (2010) 164–172.
[16] Y. Shi, E. Xing, X. Gao, D. Liu, W. Xie, F. Zhang, X. Mu, X. Shu, Topology reconstruction from FAU to MWW structure, Microporous Mesoporous Mater. 200 (2014) 269–278.
[17] L. Van Tendeloo, E. Gobechiya, E. Breynaert, J.A. Martens, C.E.A. Kirschhock, Alkaline cations directing the transformation of FAU zeolites into five different framework types, Chem. Commun. 49 (2013) 11737–11739.
[18] K. Honda, M. Itakura, Y. Matsuura, A. Onda, Y. Ide, M. Sadakane, T. Sano, Role of structural similarity between starting zeolite and product zeolite in the interzeolite conversion process, J. Nanosci. Nanotechnol. 13 (2013) 3020–3026.
[19] D. Verboekend, J. Pérez-Ramírez, Design of hierarchical zeolite catalysts by desilication, Catal. Sci. Technol. 1 (2011) 879–890.
[20] J. Pérez-Ramírez, C.H. Christensen, K. Egeblad, C.H. Christensen, J.C. Groen, Hierarchical zeolites: enhanced utilisation of microporous crystals in catalysis by advances in materials design, Chem. Soc. Rev. 37 (2008) 2530–2542.
[21] S. Mitchell, A.B. Pinar, J. Kenvin, P. Crivelli, J. Kärger, J. Pérez-Ramírez, Structural analysis of hierarchically organized zeolites, Nat. Commun. 6 (2015) 8633.
[22] D.P. Serrano, J.M. Escola, P. Pizarro, Synthesis strategies in the search for hierarchical zeolites, Chem. Soc. Rev. 42 (2013) 4004–4035.
[23] M. Müller, G. Harvey, R. Prins, Comparison of the dealumination of zeolites beta, mordenite, ZSM-5 and ferrierite by thermal treatment, leaching with oxalic acid and treatment with SiCl4 by 1H, 29Si and 27A1 MAS NMR, Microporous Mesoporous Mater. 34 (2000) 135–147.
[24] E. Catizzone, M. Migliori, A. Aloise, R. Lamberti, G. Giordano, Hierarchical low Si/Al ratio ferrierite zeolite by sequential postsynthesis treatment: catalytic assessment in dehydration reaction of methanol, J. Chem. 2019 (2019) 1–9.
[25] A. Bonilla, D. Baudouin, J. Pérez-Ramírez, Desilication of ferrierite zeolite for porosity generation and improved effectiveness in polyethylene pyrolysis, J. Catal. 265 (2009) 170–180.
[26] D. Verboekend, R. Caicedo-Realpe, A. Bonilla, M. Santiago, J. Pérez-Ramírez, Properties and functions of hierarchical ferrierite zeolites obtained by sequential post-synthesis treatments, Chem. Mater. 22 (2010) 4679–4689.
[27] R. Millini, G. Bellussi, Industrial perspectives for mesoporous zeolites, in: J. Garcia-martinez, in: K. Li (Ed.), Mesoporous Zeolites: Preparation, Characterization and Applications, Wiley-VCH Verlag GmbH & Co., KGaA, 2015, pp. 541–564.
[28] R. Chal, C. Gérardin, M. Bulut, S. VanDonk, Overview and industrial assessment of synthesis strategies towards zeolites with mesopores, ChemCatChem. 3 (2011) 67–81.
[29] W. Schwieger, A.G. Machoke, T. Weissenberger, A. Inayat, T. Selvam, M. Klumpp, A. Inayat, Hierarchy concepts: classification and preparation strategies for zeolite containing materials with hierarchical porosity, Chem. Soc. Rev. 45 (2016) 3353–3376.
[30] A. Feliczak-Guzik, Hierarchical zeolites: synthesis and catalytic properties, Microporous Mesoporous Mater. 259 (2018) 33–45.
[31] X. Zhu, R. Rohling, G. Filonenko, B. Mezari, J.P. Hofmann, S. Asahina, E.J.M. Hensen, Synthesis of hierarchical zeolites using an inexpensive mono-quaternary ammonium surfactant as mesoporogen, Chem. Commun. 50 (2014) 14658–14661.
[32] F.S. Xiao, L. Wang, C. Yin, K. Lin, Y. Di, J. Li, R. Xu, D.S. Su, R. Schlögl, T. Yokoi, T. Tatsumi, Catalytic properties of hierarchical mesoporous zeolites templated with a mixture of small organic ammonium salts and mesoscale cationic polymers, Angewandte Chemie - International Edition. 45 (2006) 3090–3093.
[33] L. Meng, X. Zhu, W. Wannapakdee, R. Pestman, M.G. Goesten, L. Gao, A.J.F. van Hoof, E.J.M. Hensen, A dual-templating synthesis strategy to hierarchical ZSM-5 zeolites as efficient catalysts for the methanol-to-hydrocarbons reaction, J. Catal. 361 (2018) 135–142.
[34] T. Xue, H. Liu, Y.M. Wang, Synthesis of hierarchical ferrierite using piperidine and tetramethylammonium hydroxide as cooperative structure-directing agents, RSC Adv. 5 (2015) 12131–12138.
[35] P. Wuamprakhon, C. Wattanakit, C. Warakulwit, T. Yutthalekha, W. Wannapakdee, S. Ittisanronnachai, J. Limtrakul, Direct synthesis of hierarchical ferrierite nanosheet assemblies via an organosilane template approach and determination of their catalytic activity, Microporous Mesoporous Mater. 219 (2016) 1–9.
[36] W. Chu, X. Li, X. Zhu, S. Xie, C. Guo, S. Liu, F. Chen, L. Xu, Size-controlled synthesis of hierarchical ferrierite zeolite and its catalytic application in 1-butene skeletal isomerization, Microporous Mesoporous Mater. 240 (2017) 189–196.
[37] Y. Lee, M.B. Park, P.S. Kim, A. Vicente, C. Fernandez, I.S. Nam, S.B. Hong, Synthesis and catalytic behavior of ferrierite zeolite nanoneedles, ACS Catal. 3 (2013) 617–621.
[38] V.J. Margarit, M.R. Díaz-Rey, M.T. Navarro, C. Martínez, A. Corma, Direct synthesis of nano-ferrierite along the 10-Ring-Channel direction boosts their catalytic behavior, Angewandte Chemie – Int. Ed. 57 (2018) 3459–3463.
[39] Y. Wang, Y. Gao, W. Chu, D. Zhao, F. Chen, X. Zhu, X. Li, S. Liu, S. Xie, L. Xu, Synthesis and catalytic application of FER zeolites with controllable size, J. Mater. Chem. A 7 (2019) 7573–7580.
[40] A. Bolshakov, M. van Diepen, A.J.F. van Hoof, D.E. Romero Hidalgo, N. Kosinov, E.J.M. Hensen, Hierarchically porous (alumino)silicates prepared by an imidazole-based surfactant and their application in acid-catalyzed reactions, ACS Appl. Mater. Interfaces (2019), https://doi.org/10.1021/acsami.9b15593.
[41] M. Isobe, T. Moteki, S. Tanahashi, R. Kimura, Y. Kamimura, K. Itabashi, T. Okubo, Plate-like precursors formed in crystallization process of ferrierite from (Na, K)-aluminosilicate system, Microporous Mesoporous Mater. 158 (2012) 204–208.
[42] T. Sano, M. Itakura, M. Sadakane, High potential of interzeolite conversion method for zeolite synthesis, J. Jpn. Pet. Inst. 56 (2013) 183–197.
[43] A. Bolshakov, D.E. Romero Hidalgo, A.J.F. van Hoof, N. Kosinov, E.J.M. Hensen, Mordenite nanorods prepared by an inexpensive pyrrolidine-based mesoporogen for alkane hydroisomerization, ChemCatChem. 11 (2019) 2803–2811.
[44] H. Robson, Verified Syntheses of Zeolitic Materials, (2016).
[45] Z. Zhao, W. Zhang, P. Ren, X. Han, U. Müller, B. Yilmaz, M. Feyen, H. Gies, F.S. Xiao, D. De Vos, T. Tatsumi, X. Bao, Insights into the topotactic conversion process from layered silicate RUB-36 to FER-type zeolite by layer reassembly, Chem. Mater. 25 (2013) 840–847.
[46] L. Schreyeck, P. Caullet, J.C. Mougenel, J.L. Guth, B. Marler, PREFER: A new layered (alumino) silicate precursor of FER-type zeolite, Microporous Mater. 6 (1996) 259–271.
[47] F. Zeolites, M. Moliner, M.E. Davis, Impact of controlling the site distribution of Al

atoms on catalytic properties in, J. Phys. Chem. C. 115 (2011) 1096–1102.
[48] H. Jongkind, K.P. Datema, S. Nabuurs, A. Seive, W.H.J. Stork, Synthesis and characterisation of zeolites using saturated cyclic amines as structure-directing agents, Microporous Mater. 10 (1997) 149–161.
[49] B.A. Holmberg, H. Wang, Y. Yan, High silica zeolite Y nanocrystals by dealumination and direct synthesis, Microporous Mesoporous Mater. 74 (2004) 189–198.
[50] J.E. Schmidt, M.A. Deimund, D. Xie, M.E. Davis, Synthesis of RTH-type zeolites using a diverse library of imidazolium cations, Chem. Mater. 27 (2015) 3756–3762.
[51] A.B. Pinar, C. Márquez-Álvarez, M. Grande-Casas, J. Pérez-Pariente, Template-controlled acidity and catalytic activity of ferrierite crystals, J. Catal. 263 (2009) 258–265.
[52] M. Thommes, K. Kaneko, A.V. Neimark, J.P. Olivier, F. Rodriguez-Reinoso, J. Rouquerol, K.S.W. Sing, Physisorption of gases, with special reference to the evaluation of surface area and pore size distribution (IUPAC Technical Report), Pure Appl. Chem. 87 (2015) 1051–1069.
[53] S. Storck, H. Bretinger, W.F. Maier, Characterization of micro- and mesoporous solids by physisorption methods and pore-size analysis, Appl. Catal. A Gen. 174 (1998) 137–146.
[54] J. Shi, M.W. Anderson, S.W. Carr, Direct observation of zeolite a synthesis by in situ solid-state NMR, Chem. Mater. 8 (1996) 369–375.
[55] L. Mafra, J.A. Vidal-Moya, T. Blasco, Structural characterization of zeolites by advanced solid State NMR spectroscopic methods, in: G.A. Webb (Ed.), Annual Reports On NMR Spectroscopy, 77 Elsevier Ltd., 2012, pp. 259–351.
[56] J.A. Van Bokhoven, D.C. Koningsberger, P. Kunkeler, H. Van Bekkum, A.P.M. Kentgens, Stepwise dealumination of zeolite Beta at specific T-sites observed with ^{27}Al MAS and ^{27}Al MQ MAS NMR, J. Am. Chem. Soc. 122 (2000) 12842–12847.
[57] T.H. Chen, B.H. Wouters, P.J. Grobet, Aluminium coordinations in zeolite mordenite by 27Al multiple quantum mas NMR spectroscopy, Eur. J. Inorg. Chem. 2 (2000) 281–285.
[58] V.L. Zholobenko, D.B. Lukyanov, J. Dwyer, W.J. Smith, Ferrierite and SUZ-4 Zeolite: Characterization of Acid Sites, J. Phys. Chem. B 102 (2002) 2715–2721.
[59] G. Onyestyák, Comparison of butene skeletal isomerization selectivity over a pair of commercial H-ferrierites, Microporous Mesoporous Mater. 104 (2007) 192–198.
[60] A. Zecchina, S. Bordiga, G. Spoto, D. Scarano, G. Petrini, G. Leofanti, M. Padovan, C.O. Areàn, Low-temperature Fourier-transform infrared investigation of the interaction of CO with nanosized ZSM5 and silicalite, Journal of the Chemical Society, Faraday Transactions. 88 (1992) 2959–2969.
[61] W. Unger, Spectroscopy in catalysis, Zeitschrift Für Physikalische Chemie. 186 (2011) 268–269.
[62] H. Knözinger, Infrared spectroscopy for the characterization of surface acidity and basicity, in: G.W. Ertl, H. Knözinger, F.J. Schüth (Eds.), Handbook of Heterogeneous Catalysis, Wiley-VCH Verlag GmbH & Co., KGaA, 2008, pp. 1135–1163.
[63] C. Márquez-Alvarez, A.B. Pinar, R. García, M. Grande-Casas, J. Pérez-Pariente, Influence of Al distribution and defects concentration of ferrierite catalysts synthesized from na-free gels in the skeletal isomerization of n-butene, Top. Catal. 52 (2009) 1281–1291.
[64] J.N. Kondo, E. Yoda, H. Ishikawa, F. Wakabayashi, K. Domen, Acid property of silanol groups on zeolites assessed by reaction probe IR study, J. Catal. 191 (2000) 275–281.
[65] P. Bräuer, P.L. Ng, O. Situmorang, I. Hitchcock, C. D'Agostino, Effect of Al content on number and location of hydroxyl acid species in zeolites: a DRIFTS quantitative protocol without the need for molar extinction coefficients, RSC Adv. 7 (2017) 52604–52613.
[66] X. Zhu, J.P. Hofmann, B. Mezari, N. Kosinov, L. Wu, Q. Qian, B.M. Weckhuysen, S. Asahina, J. Ruiz-Martínez, E.J.M. Hensen, Trimodal porous hierarchical SSZ-13 zeolite with improved catalytic performance in the methanol-to-Olefins reaction, ACS Catal. 6 (2016) 2163–2177.
[67] A.A. Gabrienko, I.G. Danilova, S.S. Arzumanov, L.V. Pirutko, D. Freude, A.G. Stepanov, Direct measurement of zeolite brønsted acidity by FTIR spectroscopy: solid-state ^{1} H MAS NMR approach for reliable determination of the integrated molar absorption coefficients, J. Phys. Chem. C 122 (2018) 25386–25395.
[68] A.A. Gabrienko, I.G. Danilova, S.S. Arzumanov, A.V. Toktarev, D. Freude, A.G. Stepanov, Strong acidity of silanol groups of zeolite beta: evidence from the studies by IR spectroscopy of adsorbed CO and ^{1}H MAS NMR, Microporous Mesoporous Mater. 131 (2010) 210–216.
[69] P.M.M. Blauwhoff, Zeolites as catalysts in industrial processes, in: J. Weikamp, L. Puppe (Eds.), Catalysis and Zeolites, Springer-Verlag, Berlin Heidelberg, New York, 1999, pp. 437–538.
[70] A. Humphries, D.H. Harris, P. O'connor, The nature of active sites in zeolites: Influence on catalyst performance, Stud. Surf. Sci. Catal. 76 (1993) 41–82.
[71] J. Zhang, J. Uknalis, L. Chen, R.A. Moreau, H. Ngo, Development of magnesium oxide–Zeolite catalysts for isomerization of fatty acids, Catal. Letters 149 (2019) 303–312.
[72] S.C.C. Wiedemann, J.A. Stewart, F. Soulimani, T. Van Bergen-Brenkman, S. Langelaar, B. Wels, P. De Peinder, P.C.A. Bruijnincx, B.M. Weckhuysen, Skeletal isomerisation of oleic acid over ferrierite in the presence and absence of triphenylphosphine: pore mouth catalysis and related deactivation mechanisms, J. Catal. 316 (2014) 24–35.